Three-dimensional frequency-domain optical anisotropy imaging of biological tissues with near-infrared light

Ahmad Addoum, Sylvain Contassot-Vivier, Fatmir Asllanaj

Three-dimensional frequency-domain optical anisotropy imaging of biological tissues with near-infrared light

Ahmad Addoum[a)]
Université de Lorraine LEMTA CNRS UMR7563 ENSEM, F54500 Vandoeuvre-lès-Nancy, France

Sylvain Contassot-Vivier
Université de Lorraine LORIA CNRS UMR7503, F54506 Vandoeuvre-lès-Nancy, France

Fatmir Asllanaj
Université de Lorraine LEMTA CNRS UMR7563 ENSEM, F54500 Vandoeuvre-lès-Nancy, France

Purpose: Near-infrared optical imaging aims to reconstruct the absorption μ_a and scattering μ_s coefficients in order to detect tumors at early stage. However, the reconstructions have only been limited to μ_a and μ_s due to theoretical and computational limitations. The authors propose an efficient method of the reconstruction, in 3D geometries, of the anisotropy factor g of the Henyey-Greenstein phase function as a new optical imaging biomarker.

Methods: The light propagation in biological tissues is accurately modeled by the Radiative Transfer Equation (RTE) in the frequency domain. The reconstruction algorithm is based on a gradient-based updating scheme. The adjoint method is used to efficiently compute the gradient of the objective function which represents the discrepancy between simulated and measured boundary data. A parallel implementation is carried out to reduce the computational time.

Results: We show that by illuminating only one surface of a tissue-like phantom, the algorithm is able to accurately reconstruct optical values and different shapes (spherical and cylindrical) that characterize small tumors-like inclusions. Numerical simulations show the robustness of the algorithm to reconstruct the anisotropy factor with different contrast levels, inclusion depths, initial guesses, heterogeneous background, noise levels and two-layered medium. The crosstalk problem when reconstructing simultaneously μ_s and g has been reported and achieved with a reasonable quality.

Conclusions: The proposed RTE-based reconstruction algorithm is robust to spatially retrieve and localize small tumoral inclusions. Heterogeneities in g-factor have been accurately reconstructed which makes the new algorithm a candidate of choice to image this factor as new intrinsic contrast biomarker for optical imaging.

Keywords optical image reconstruction, anisotropy factor, cancer diagnosis, radiative transfer equation.

Introduction

Diffuse Optical Tomography (DOT) is a non-invasive imaging modality that aims to reconstruct the optical properties of biological tissues namely, the absorption μ_a and the scattering μ_s coefficients. It consists in solving the photon migration to predict the boundary light intensities through a forward model. These predictions are compared with the observed measurements, and the optical image is then iteratively updated to minimize the objective function represented by the discrepancy between predicted and observed data within an inversion scheme. An accurate forward model is essential to meet the requirements of clinical applications and to obtain a good quality reconstruction. The most commonly applied forward model in DOT is the Diffusion Equation[1] due to its ease of implementation and the wide availability of fast and efficient numerical solvers in arbitrary domains. However, this model does not accurately simulate light propagation in optically thin media or in others containing low-scattering or strong light absorption regions.[2] The drawbacks of the Diffusion Equation particularly concern small-volume tissues imaging, such as finger joints[3] and body parts in small animals due to the small source-detector separation.[4,5] It is well known that the biological tissues are highly forward scattering media where the anisotropy factor g is close to unity.[6] Several works have shown that this factor can be modified when the tissue is affected by a tumor because cells and cell nuclei change their size and shape. Therefore, the morphological modification of the tissue changes the scattering coefficient μ_s. Since the g-factor describes the anisotropy (angular distribution) of light scattering, this modification will also lead to a variation of g values between healthy and tumor tissues. For examples, Van Hillegersberg et al.[7] demonstrated that the g-factor of rat liver decreases from 0.952 to 0.946 in a tumor at 633 nm. Germer et al.[8] reported experimentally that g was different for normal human liver tissue (g = 0.902) and liver metastases (g = 0.955) at three different wave-lengths. Consequently, the g-factor can provide an additional intrinsic contrast for optical imaging. It should be noted that the determination of the anisotropy factor g is not possible using the Diffusion Equation, which is devoted to describing an isotropic fluence field. This isotropy is achieved when the photon penetration depths within the medium are large relatively to the transport mean-free path $l_{tr} = 1/\mu_s'$,[9] where $\mu_s' = \mu_s(1-g)$ is the reduced scattering coefficient. The typical penetration depth scales for which light propagation still maintains a degree of anisotropy can range from 1 to 10 mm, depend-

ing on optical values of tissues. To overcome these limitations, the Radiative Transfer Equation (RTE) has been addressed as a rigorous model for light transport in biological tissues and has become a focus of investigations. The anisotropic scattering behavior is well modeled through the RTE via the Henyey-Greenstein (H-G) phase function. However, it must be kept in mind that the RTE is difficult to solve. It requires complex computational methods which are expensive in terms of runtime and memory resources due to the spatial and angular dependence of the radiance. In two-dimensional geometries, many improvements have been made in the development of RTE-based reconstruction scheme using steady-state,[10] frequency[11] or time-resolved[12] measurements. At present, although 3D imaging is indispensable for practical settings, reconstructing the optical properties with the 3D RTE has not been sufficiently reported in the literature. This is mainly due to the excessive computational effort required in the reconstruction. To name a few, Abdoulaev et al.[13] have established a mathematical framework based on the time-independent RTE in 3D geometries. Each iteration of their reconstruction scheme took on average 35 min on a 700 MHz Pentium III XENON processor. With a similar processor, Klose et al.[14] have shown that it tooks 98 hours to reconstruct the μ_s and μ_a coefficients after only 4 iterations of a gradient-based algorithm using the 3D RTE in the steady-state domain. Ren et al.[15] have mentioned that 22 hours were needed to retrieve the optical coefficients at single-modulation frequency (600 MHz) on a 3GHz Pentium XEON processor.

The objective of this work was to develop a 3D optical imaging algorithm using an accurate forward model based on the RTE in the frequency-domain. In this study, a particular attention was devoted to reconstructing, for the first time, the g-factor as a new optical contrast biomarker in 3D geometry. For the inversion, a gradient-based scheme[16,17] using the Lm-BFGS[18] was considered to update the spatial distribution of optical properties. In such scheme, the major challenge is the computation of the objective function gradient which is the most expensive step. Evaluating the gradient through perturbation methods is daunting and prohibitively expensive with the RTE, especially in this case where the parameters are spatially dependent. To overcome this difficulty, the adjoint method was used to efficiently compute the objective function gradient with respect to the three parameters (μ_a, μ_s and g-factor) regardless the number of unknowns. The remainder of this paper is organized as follows. In Sec.1, the RTE model is presented and the predictions on semi-transparent boundaries are given. In Sec. 2, the parallel reconstruction algorithm based on the Lagrangian formalism and the Lm-BFGS optimization scheme is described.

Reconstructions results based on synthetic data are presented and discussed in Sec. 3 through different test cases. Concluding remarks are finally offered in Sec. 4.

1 Forward model

The RTE in the frequency-domain is used to accurately describe the light propagation within biological tissues. The external Laser beam $\Gamma(\boldsymbol{r_s}, \omega)$ illuminating the surface at the position $\boldsymbol{r_s}$ with the angular modulation frequency ω is seperated into two components $\psi = \psi_c + \psi_s$, respectively the collimated ψ_c and scattered radiance ψ_s. This allows taking into account the collimated radiation in our forward model. The ψ_c component is governed by the RTE state equation denoted $\mathcal{R}_c$ in the collimated direction $\boldsymbol{\Omega_c}$ and is analytically solved in accordance with the Bouguer-Beer-Lambert exponential law :

$$\mathcal{R}_c = \left[\boldsymbol{\Omega_c} \cdot \nabla + \left(\frac{i\, n\, \omega}{c} + \mu_t(\boldsymbol{r}) \right) \right] \psi_c(\boldsymbol{r}, \omega) = 0 \tag{1}$$

where c is light velocity in vacuum while n is the refractive index of tissue. The total extinction coefficient $\mu_t(\boldsymbol{r})$, at position $\boldsymbol{r}$, represents the sum of the absorption $\mu_a(\boldsymbol{r})$ and the scattering $\mu_s(\boldsymbol{r})$ coefficients. The tissue surfaces are modeled as semi-transparent boundaries due to the refractive index mismatch between air and tissue. The boundary condition for the collimated radiance is thus given by :

$$\psi_c(\boldsymbol{r_s}, \omega) = [1 - R(\Theta')]\, \Gamma(\boldsymbol{r_s}, \omega) \quad \text{for} \quad \boldsymbol{\Omega_c} \cdot \boldsymbol{n_{out}} < 0, \tag{2}$$

where $\boldsymbol{n_{out}}$ is the local outward unit vector normal to the tissue boundary. The reflectivity coefficient R depends on the incidence angle Θ', with $\cos\,\Theta' = \boldsymbol{\Omega'} \cdot \boldsymbol{n_{out}}$, and where the incident direction $\boldsymbol{\Omega'}$ satisfied $\boldsymbol{\Omega'} \cdot \boldsymbol{n_{out}} > 0$. Once the $\mathcal{R}_c$ equation is solved, the solution ψ_c is then used through a source term S_c such as :

$$S_c(\boldsymbol{r}, \boldsymbol{\Omega}, \omega) = \mu_s(\boldsymbol{r})\, p(\boldsymbol{r}, \boldsymbol{\Omega_c} \cdot \boldsymbol{\Omega})\, \psi_c(\boldsymbol{r}, \omega) \tag{3}$$

where $p(\boldsymbol{r}, \boldsymbol{\Omega'} \cdot \boldsymbol{\Omega})$ is the Henyey-Greenstein (H-G) phase function which represents the probability that photon traveling in incident direction $\boldsymbol{\Omega'}$ deviates into scattering direction $\boldsymbol{\Omega}$. Its mathematical expression in 3D participating

media[19] is given by :

$$p(\boldsymbol{r}, \boldsymbol{\Omega'} \cdot \boldsymbol{\Omega}) \;=\; \frac{1}{4\pi} \frac{1 - g^2(\boldsymbol{r})}{\left(1 + g^2(\boldsymbol{r}) - 2\, g(\boldsymbol{r})\, \boldsymbol{\Omega'} \cdot \boldsymbol{\Omega}\right)^{3/2}} \tag{4}$$

where g is the anisotropy factor characterizing the angular distribution of tissue scattering. In this study, g is space-dependent. Hence, in addition to the dependence of the phase function p on the incident and scattered directions through an inner product, p is also a function of the spatial position $\boldsymbol{r}$ (see Eq. 4). The coupling term S_c (Eq. 3) is included within the RTE state equation $\mathcal{R}_s$ which governs the scattered radiance ψ_s in the direction $\boldsymbol{\Omega}$:

$$\begin{aligned} \mathcal{R}_s = \left[\boldsymbol{\Omega} \cdot \nabla + \left(\frac{i\, n\, \omega}{c} + \mu_t(\boldsymbol{r}) \right) \right] \psi_s(\boldsymbol{r}, \boldsymbol{\Omega}, \omega) \\ -\mu_s(\boldsymbol{r}) \int_{\Omega'=4\pi} p(\boldsymbol{r}, \boldsymbol{\Omega}^{'} \cdot \boldsymbol{\Omega})\, \psi_s(\boldsymbol{r}, \boldsymbol{\Omega}^{'}, \omega)\, d\Omega^{'} - S_c(\boldsymbol{r}, \boldsymbol{\Omega}, \omega) = 0 \end{aligned} \tag{5}$$

The detected signals correspond to the outgoing fluence predicted at the detector position $\boldsymbol{r_d}$ on the illuminated bounding surface such as :

$$P(\boldsymbol{r_d}, \omega) \;=\; \int_{\boldsymbol{\Omega'} \cdot \boldsymbol{n_{out}} > 0} \left[1 - R(\Theta')\right] \psi_s(\boldsymbol{r_d}, \boldsymbol{\Omega'}, \omega) \left(\boldsymbol{\Omega'} \cdot \boldsymbol{n_{out}}\right) d\Omega' \tag{6}$$

The angular space was uniformly subdivided into several discrete directions. The deterministic numerical method used in this study for solving the RTE is based on the Modified Finite Volume Method (MFVM). This method can benefit from the efficient inversion techniques (based for example on the adjoint method presented in the next section) developed specifically for partial differential equations. The "modified" word is due to the fact the photon transport is solved even inside each control volume within an exponential scheme. The MFVM is thus qualified as a highly accurate method compared to other deterministic numerical methods available in the literature. Relative differences of less than 1.5% were obtained in comparison with the Monte-Carlo reference solution for some selected problems.[20] The methodology of the employed method is not repeated here, we refer the reader to [20] for comprehensive details.

2 Inverse problem

2.1 Lagrangian formalism and adjoint model

The inverse problem can be considered as a large-scale optimization problem which consists to minimize the least-square discrepancy between the measurements $M(\boldsymbol{r}_d, \omega)$ and the forward model predictions $P(\boldsymbol{r}_d, \omega)$ at the detector position $\boldsymbol{r}_d$ and angular frequency ω. These discrepancies are represented by a real-valued non-negative function, called the objective function defined by :

$$\mathcal{J}(\boldsymbol{\beta}, \omega) = \sum_{d=1}^{N_d} \left|\left|P(\boldsymbol{r}_d, \omega) - M(\boldsymbol{r}_d, \omega)\right|\right|_2^2 \tag{7}$$

where $||\cdot||_2$ denotes Euclidean norm. The vector $\boldsymbol{\beta}$ contains the spatial distribution of optical properties to be reconstructed and N_d is the total number of detectors on the tissue surface. The objective is to determine the vector $\hat{\boldsymbol{\beta}}$ that minimizes this function and vanishes the gradient $\nabla\mathcal{J}(\hat{\boldsymbol{\beta}}, \omega) = 0$. In this work, instead of solving the unconstrained problem (Eq. 7), we adopted an adjoint method that solves the constrained optimization problem by following the Lagrangian formalism given as :

$$\mathcal{L}(\boldsymbol{\beta}, \psi_s, \psi_c, \lambda_s, \lambda_c) = \mathcal{J}(\boldsymbol{\beta}, \omega) + \left\langle \lambda_s \middle| \mathcal{R}_s(\boldsymbol{\beta}, \psi_s, \psi_c) \right\rangle_s + \left\langle \lambda_c \middle| \mathcal{R}_c(\boldsymbol{\beta}, \psi_c) \right\rangle_c \tag{8}$$

where λ_s and λ_c are respectively the Lagrange multipliers to ψ_s and ψ_c. $\langle\cdot|\cdot\rangle_s$ and $\langle\cdot|\cdot\rangle_c$ denote the inner products associated to the solution space of ψ_s and ψ_c, respectively.[21]

$$\left\langle \lambda_s \middle| \mathcal{R}_s(\boldsymbol{\beta}, \psi_s, \psi_c) \right\rangle_s = \mathfrak{Re} \int_{\mathcal{D}} \int_{\boldsymbol{\Omega}=4\pi} \overline{\lambda_s(\boldsymbol{r}, \boldsymbol{\Omega}, \omega)} \mathcal{R}_s(\boldsymbol{\beta}, \psi_s, \psi_c) d\Omega dr \tag{9}$$

$$\left\langle \lambda_c \middle| \mathcal{R}_c(\boldsymbol{\beta}, \psi_c) \right\rangle_c = \mathfrak{Re} \int_{\mathcal{D}} \overline{\lambda_c(\boldsymbol{r}, \boldsymbol{\Omega}, \omega)} \mathcal{R}_s(\boldsymbol{\beta}, \psi_c) dr \tag{10}$$

The objective function (Eq. 7) is minimized under some equality constraints ($\mathcal{R}_c = 0$ and $\mathcal{R}_s = 0$) based on the RTE state equations. The optimization problem consists to find the stationary point (vector solution $\hat{\boldsymbol{\beta}}$) of the Lagrangian function (Eq. 8) that vanishes its gradient $\nabla\mathcal{L}$ with respect to all its variables $\nabla_{\lambda_{s,c}}\mathcal{L} = \nabla_{\psi_{s,c}}\mathcal{L} = \nabla_{\beta}\mathcal{L} = 0$. Using

the adjoint operator[22] and the inner product properties, the differentiation of $\mathcal{L}$ with respect to the state variables ψ_s and ψ_c ($\nabla_{\psi_{s,c}}\mathcal{L}$) leads to the RTE adjoint equations for the scattered and collimated components, respectively :

$$\left[-\boldsymbol{\Omega}\cdot\nabla+\left(\frac{-i\omega}{c/n}+\mu_t(\boldsymbol{r})\right)\right]\lambda_s(\boldsymbol{r},\boldsymbol{\Omega},\omega)=\mu_s(\boldsymbol{r})\int_{4\pi}p(\boldsymbol{r},\boldsymbol{\Omega'}\cdot\boldsymbol{\Omega})\,\lambda_s(\boldsymbol{r},\boldsymbol{\Omega}',\omega)\,d\boldsymbol{\Omega'}-\frac{\partial\mathcal{J}(\boldsymbol{\beta},\omega)}{\partial\psi_s} \tag{11}$$

$$\left[-\boldsymbol{\Omega}_c\cdot\nabla+\left(\frac{-i\,\omega}{c/n}+\mu_t(\boldsymbol{r})\right)\right]\lambda_c(\boldsymbol{r},\omega)=\mu_s(\boldsymbol{r})\int_{4\pi}p(\boldsymbol{r},\boldsymbol{\Omega_c}\cdot\boldsymbol{\Omega})\,\lambda_s(\boldsymbol{r},\boldsymbol{\Omega},\omega)\,d\boldsymbol{\Omega} \tag{12}$$

Note that $\nabla_{\psi_c}\mathcal{J}(\boldsymbol{\beta},\omega)=0$ because the objective function is independent of the collimated light. The Lagrange multipliers λ_s and λ_c are solutions to (Eq. 11) and (Eq. 12), respectively. The above system was derived in details in our previous study[21] based on 2D geometries. Note that, in 3D geometries, the integral term over 2π is replaced by the integral term over 4π. One major advantage of this approach is its simple implementation by applying the same numerical solver as used for the forward model. Furthermore, the adjoint method provides the gradient of the objective function in a fast and efficient way (independently of the number of unknown parameters). Once the adjoint equations are solved and the Lagrange multipliers are obtained, the latter are then used to compute the gradient ($\nabla_\beta\mathcal{J}$) with a computational time equivalent to a one forward simulation.

2.2 Gradient expressions

The directional derivative $\mathcal{L}'$ of the Lagrangian (Eq. 8) represents the inner product of its gradient $\nabla\mathcal{L}(\boldsymbol{\beta})$ with respect to $\boldsymbol{\beta}$ in the direction $\delta\boldsymbol{\beta}$. Differentiating Eq. 8 with respect to $\boldsymbol{\beta}$, the $\mathcal{L}'$ can be expressed such that:

$$\mathcal{L}'(\boldsymbol{\beta})=\Big\langle\nabla\mathcal{L}(\boldsymbol{\beta})\Big|\delta\boldsymbol{\beta}\Big\rangle_{L_2}=\Big\langle\lambda_s\Big|\frac{\partial\mathcal{R}_s(\boldsymbol{\beta},\psi_s,\psi_c)}{\partial\beta}\delta\boldsymbol{\beta}\Big\rangle_s+\Big\langle\lambda_c\Big|\frac{\partial\mathcal{R}_c(\boldsymbol{\beta},\psi_c)}{\partial\beta}\delta\boldsymbol{\beta}\Big\rangle_c \tag{13}$$

Note that $\frac{\partial\mathcal{J}(\boldsymbol{\beta})}{\partial\boldsymbol{\beta}}=0$ since the function $\mathcal{J}(\boldsymbol{\beta},\omega)$ depends implicitly on $\boldsymbol{\beta}$ (see Eq. 7). When the radiance ψ_s and ψ_c verify the constraints equations $\mathcal{R}_s=0$ and $\mathcal{R}_c=0$, that leads to $\mathcal{L}(\boldsymbol{\beta})=\mathcal{J}(\boldsymbol{\beta})$ and thus $\mathcal{L}'(\boldsymbol{\beta})=\mathcal{J}'(\boldsymbol{\beta})$. The gradient $\nabla\mathcal{J}(\boldsymbol{\beta})$ can then be extracted from the latter expression (Eq. 13) which shows that only a simple inner product has to be calculated. This gradient is directly computed by partially differentiating the RTE state equations $\mathcal{R}_s$ and $\mathcal{R}_c$ with respect to $\boldsymbol{\beta}$ in the direction $\delta\boldsymbol{\beta}$. Applying now Eq. (13) for μ_a, μ_s and g, we obtain the analytical

gradient expressions with respect to the three optical parameters which are a function of spatial positions, $\boldsymbol{r}$, only:

$$\nabla_{\mu_a}\mathcal{J}(\boldsymbol{\beta},\omega) = \mathfrak{Re}\int_{\boldsymbol{\Omega}=4\pi}\overline{\lambda_s(\boldsymbol{r},\boldsymbol{\Omega},\omega)}\psi_s(\boldsymbol{r},\boldsymbol{\Omega},\omega)d\boldsymbol{\Omega} + \overline{\lambda_c(\boldsymbol{r},\omega)}\psi_c(\boldsymbol{r},\omega) \tag{14}$$

$$\nabla_{\mu_s}\mathcal{J}(\boldsymbol{\beta},\omega) = \nabla_{\mu_a}\mathcal{J}(\boldsymbol{\beta},\omega) - \mathfrak{Re}\int_{\boldsymbol{\Omega}=4\pi}\overline{\lambda_s(\boldsymbol{r},\boldsymbol{\Omega},\omega)}\Bigg(\int_{\boldsymbol{\Omega'}=4\pi}\psi_s(\boldsymbol{r},\boldsymbol{\Omega'},\omega)p(\boldsymbol{r},\boldsymbol{\Omega'}\cdot\boldsymbol{\Omega})d\Omega' + \psi_c(\boldsymbol{r},\omega)p(\boldsymbol{r},\boldsymbol{\Omega}_c\cdot\boldsymbol{\Omega})\Bigg)d\boldsymbol{\Omega} \tag{15}$$

$$\nabla_g\mathcal{J}(\boldsymbol{\beta},\omega) = -\mathfrak{Re}\int_{\boldsymbol{\Omega}=4\pi}\overline{\lambda_s(\boldsymbol{r},\boldsymbol{\Omega},\omega)}\mu_s(\boldsymbol{r})\Bigg(\psi_c(\boldsymbol{r},\omega)\frac{\partial p(\boldsymbol{r},\boldsymbol{\Omega}_c\cdot\boldsymbol{\Omega})}{\partial g} + \int_{\boldsymbol{\Omega'}=4\pi}\psi_s(\boldsymbol{r},\boldsymbol{\Omega'},\omega)\frac{\partial p(\boldsymbol{r},\boldsymbol{\Omega'}\cdot\boldsymbol{\Omega})}{\partial g}d\Omega'\Bigg)d\boldsymbol{\Omega} \tag{16}$$

The derivative of the H-G phase function with respect to the g-factor is evaluated analytically. At each inversion iteration, the forward and adjoint models are solved and the gradient is accurately obtained accordingly to the above expressions. The latter is then used to compute the gradient-descend direction d based on the Limited-memory BFGS method[23] to iteratively update the spatial distribution of the optical properties $\boldsymbol{\beta}$ such as:

$$\boldsymbol{\beta}^{k+1} = \boldsymbol{\beta}^k + \alpha^k\, d(\nabla\mathcal{J}^k(\boldsymbol{\beta},\omega)) \tag{17}$$

where k is the current iteration of the inverse procedure and α^k represents the step size obtained by the *Armijo* line search[18] in order to provide a sufficient minimization of the objective function. The reconstruction of the anisotropy factor g in 3D media is expected to be extremely expensive in terms of time and memory since the H-G phase function p depends on $\boldsymbol{r}$ = (x, y, z), $\boldsymbol{\Omega'}$ and $\boldsymbol{\Omega}$. In order to render possible the g reconstruction, parallel implementation in the present algorithm was unavoidable.

2.3 Parallel computing

It is clear that exploiting the RTE model, within an iterative procedure, to reconstruct the optical properties for 3D geometries can take long computational time. Thus, we implemented a multi-threading parallel algorithm. At this

level, multiple threads computed the RTE along different directions. It should be pointed out that the H-G phase function was calculated only once when the medium was assumed to be homogeneous in g-factor. On the other hand, when this factor has to be reconstructed (g-factor varies spatially inside the medium), the H-G phase function and also its derivative (required for the gradient $\nabla_g \mathcal{J}$) must be evaluated at every spatial node and overall incident and scattered directions of light propagation. In addition to the extensive computational time, the resulting values necessitate huge memory space which may exceed the capacity of a single machine. In this regard, our algorithm was extended to support multiple machines, via explicit Messages Passing Interface (MPI). In this context, some of the data were distributed over the machines of the computing system and data exchanges were performed between them for the computations that require all the data.

3 Results and discussion

3.1 Model description

The three-dimensional numerical phantom used for reconstruction is a cube of length 1 cm. It contains a spherical tumor like-inclusion with 2 mm of diameter centered at $X = Y = Z = 2$ mm (Fig. 1). The latter is embedded in a homogeneous background medium with $\mu_a = 0.01$ mm^{-1}, $\mu_s = 2$ mm^{-1} and $g = 0.8$. These are typical values of the optical properties of biological tissues in the near-infrared spectral range. The refractive index of the medium is uniformly set at $n = 1.4$ while that of the surrounding medium (air) is set to unity.

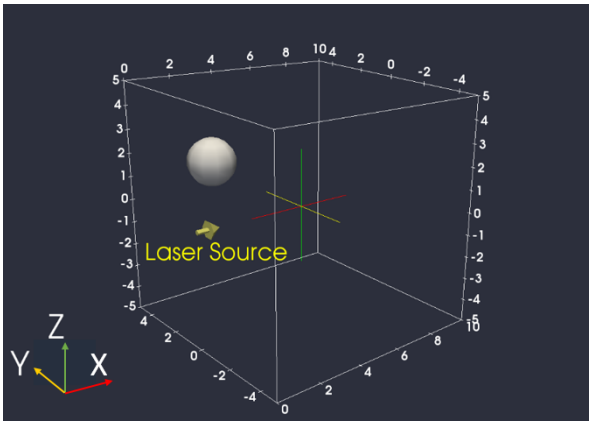

Figure 1: Original cubic phantom of length 10 mm. A spherical tumoral inclusion is embedded in a background medium. A Gaussian Laser beam illuminates the origin of the western surface of the medium (yellow arrow).

The optical properties of the inclusion were set to (μ_a, $2\mu_s$, g) relative to the background. For the first three test

cases, the μ_a coefficient and the g-factor are assumed to be constant in the medium. The reconstructions of the medium were performed with a structured mesh of 269,001 nodes (degrees of freedom) and 1,536,000 tetrahedral elements. The angular space (4πSr) was uniformly discretized into 64 control solid angles and each angle was also subdivided into 8 azimuthal and polar directions for the phase function normalization.[24] A Gaussian Laser source is used to illuminate the western surface (x = 0 mm) of the medium. The expression of the spatial Gaussian function along the y- axis and z- axis is given by :

$$\Upsilon(r) = \frac{2}{\pi\ \sigma_s^2} \exp\big(\frac{-2\|r - r_s\|_2^2}{\sigma_s^2}\big), \tag{18}$$

where σ_s = 0.5 mm is the standard deviation of the Laser beam. The spatial position $r_s = (0, r_{sy}, r_{sz})$ corresponds to the source location at the peak intensity. For all the test cases presented further, only the backscattered light (reflectance) on the illuminated boundary is used for reconstruction. This configuration allows to better simulate the experimental set-up based on the reflected mode measurements. 800 complex intensities were synthesized by running the forward model on a finer mesh of 1,081,665 nodes in order to avoid the inverse crime. These intensities correspond to the absolute fluence rate containing the amplitude and phase of the modulation frequency. Each measurement point is spatially represented by five mesh nodes on the western surface to assign a realistic detector dimension. These data are contaminated with 1% of Gaussian random noise and given as an input in the reconstruction algorithm. The inversion procedure was started with an initial guess corresponding to the homogeneous background. It terminated after the normalized difference of the objective function between two subsequent iterations was smaller than a prescribed value, here equal to 10^{-5}. The quality reconstruction of the inclusion was determined thanks to the relative error ε between exact (β^*) and estimated ($\hat{\beta}$) values such as :

$$\varepsilon = 100\%.\frac{||\hat{\beta} - \beta^*||_2}{||\beta^*||_2} \tag{19}$$

The reconstructions were carried out on a cluster with ten nodes Intel Xeon X5650 of 2.66 GHz / 12 Threads (4.75 GFlops per core), 48 Go RAM.

In the first test, the collimated source was placed at the origin of the western surface (Fig. 1). The source was mod-

ulated at 600 MHz since high frequencies are known to be suitable for probing small volume imaging. However, it is worth noting that the detectors are usually more sensitive and less noisy at low frequencies range [50 - 200 MHz]. The convergence criterion was satisfied after 19 iterations of the inversion procedure. The reconstructed medium crossed by the y = 2 mm plane is depicted on Fig. 2a. Figure 2b shows the slice in the z = 2 mm plane of the estimated μ_s coefficient.

(a) (b)

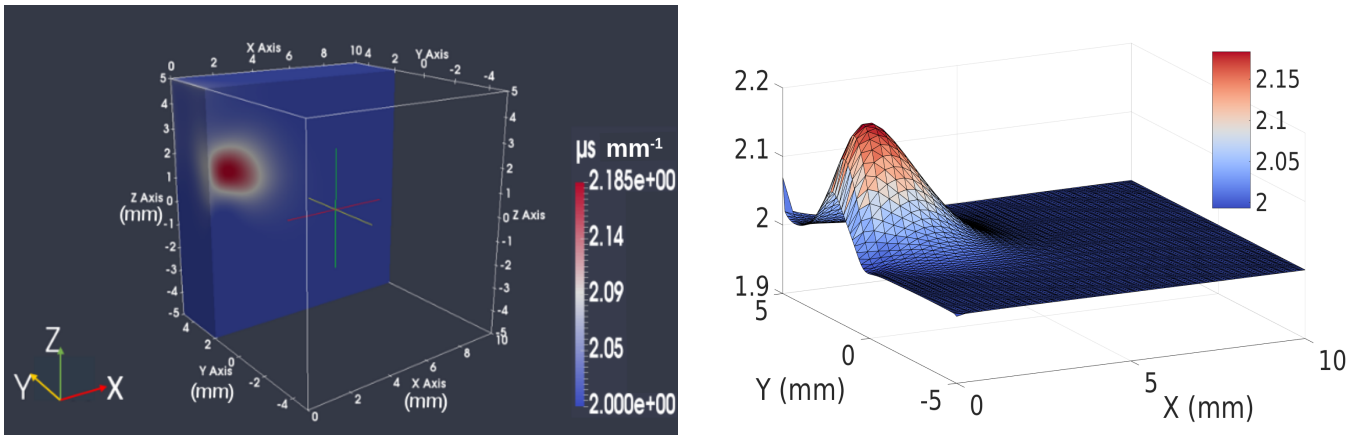

Figure 2: Reconstructed μ_s image for the first test case : one frequency modulation (600 MHz). (a) shows the slice at y = 2 mm plane (b) represents the slice in the z = 2 mm plane.

Despite the simulation conditions (one source at a fixed position with a single modulation frequency), the reconstruction algorithm has successfully revealed the region of interest (the tumor) and has correctly recovered the background medium. The center position of the reconstructed inclusion was found at y_{inc} = 1.45 mm and z_{inc} = 1.65 mm. This is an important qualitative indication allowing to localize the inclusion around the y-z positive area without a priori knowledge. However, the μ_s coefficient values of the inclusion (ε = 47.60 %) were very underestimated where the maximum value retrieved has reached only 2.18 mm^{-1} against 4 mm^{-1}. This is mainly due to the under-determinate nature of the inverse problem where 800 boundary data were insufficient to reconstruct 269,000 unknowns at each grid node of the cubic phantom. Moreover, the reconstructed shape (sphere) is elongated and placed very close to the boundary domain. Therefore, the inclusion depth ($x_{inc} \approx 0.9$ mm) was achieved with a poor quality localization.

It has been demonstrated that the image reconstruction quality in the optical tomography can be significantly improved by using large data sets in the reconstruction.[25] To this end, the multi-frequency approach[26] was considered

for the second test case. The source intensity was modulated at five frequencies equally distributed by 200 MHz and switched from 200 MHz to 1 GHz. This range is typical for DOT applications especially when high-frequencies are needed to probe superficial domains.[15,25,27] The obtained image is shown in Fig. 3.

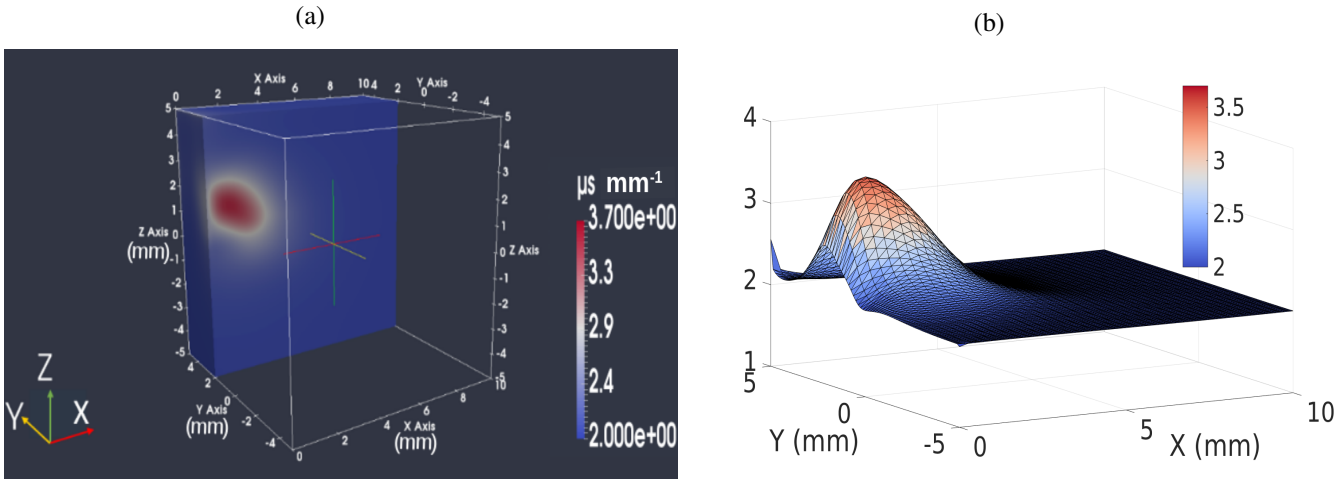

Figure 3: Reconstructed μ_s image for the second test case : five modulation frequency equally distributed. (a) shows the slice at y = 2 mm plane (b) represents the slice in the z = 2 mm.

The reconstruction quality of the inclusion was improved. Indeed, the relative error has been decreased to ε = 30.41 $\%$ where the maximum retrieved value inside the inclusion has reached 3.7 mm^{-1} against 4 mm^{-1} (Fig. 3a). One can deduce that the single frequency approach may provide a qualitative image whereas the multi-frequency approach provides the quantitative accuracy required for phantoms characterization. However, the computation cost with the second approach is more expensive. The μ_s image was reconstructed after 22 hours using 5 frequencies while it took only 4 hours to obtain the μ_s image at 600 MHz. In addition, even with more boundary data sets, the present illumination configuration is unable to accurately reconstruct the depth localization, shape, and size of the inclusion. While its center is found at approximately the right position (y_{inc} = 1.9 mm and z_{inc} = 1.9 mm) along the y and z axis, the location in depth ($x_{inc} \approx$ 1 mm) remains under-estimated with respect to the target position. This behavior is commonly encountered in optical imaging since the light sensitivity drops off severely and quickly with depth, leading to a significant position error. To overcome this issue, as a third test case, the Laser source was displaced to illuminate the positive region along the y - and z - axis where the peak intensity is now located at (0, 1, 1). In this case, one modulation frequency (600 MHz) was used. The results are presented in Fig. 4.

It is seen that the algorithm has now recovered the volumetric image location with good accuracy and high contrast

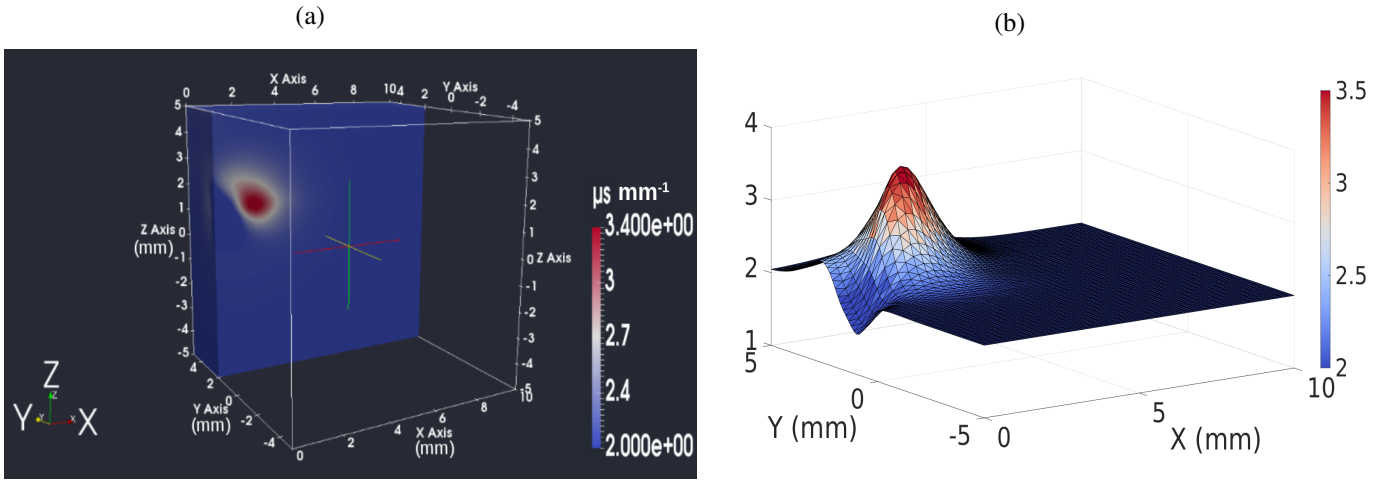

Figure 4: Reconstructed μ_s image for the third test case : one modulation frequency (600 MHz) and when the Laser source is placed near to the inclusion (0, 1, 1). (a) shows the slice at y = 2 mm plane (b) represents the slice in the z = 2 mm plane.

after about 4 hours. The retrieved μ_s values inside the inclusion have reached approximately 75% of their target value. In this case, the localization in depth of the reconstructed inclusion has somehow reached the correct value (x $\approx$ 2 mm), contrary to the previous cases. Moreover, the inclusion was reconstructed with a good spherical shape and size. Therefore, the relative error of the inclusion was enhanced (ε = 15.86 %) even though one single frequency with one source were considered. These improvements can be explained by the localization of the heterogeneity in a high sensitivity region with respect to the collimated source. It should be noted that the result was obtained without adding a prior spatial information within the algorithm. The light source was only moved toward the region including the heterogeneity. This configuration is an alternative strategy providing a good compromise between quantitative accuracy and computational time. That can be ensured by illuminating the medium from any point on the surface as a first step and once the suspected area is identified (test case 1), the Laser source can then be positioned nearer to the inclusion (test case 3) as a second step. This procedure allows performing tomographic reconstructions without having to probe the medium with multiple sources at different boundaries positions or with multiple-frequencies. Moreover, it avoids combining prior knowledge provided by another imaging modalities such as MRI[28] or X-Ray[29] by exclusively exploiting the qualitative indication obtained by our reconstruction algorithm. The simultaneous reconstruction of μ_a and μ_s was carried out in the fourth test case. In this case, the g-factor is fixed at its homogeneous background value. Here, we used the same original phantom (see Fig. 1) which was illuminated as in the third test case. The spherical inclusion represents a high contrast heterogeneity where the

optical properties are set to ($2\mu_a$, $2\mu_s$, g) relative to the background values. The reconstructed and exact profiles of μ_a and μ_s passing through the center of the inclusion (2, 2, 2) along the x, y and z axis are shown in Fig. 5. These profiles allow highlighting the location precision, the depth (along the x - axis), the size and the quantitative

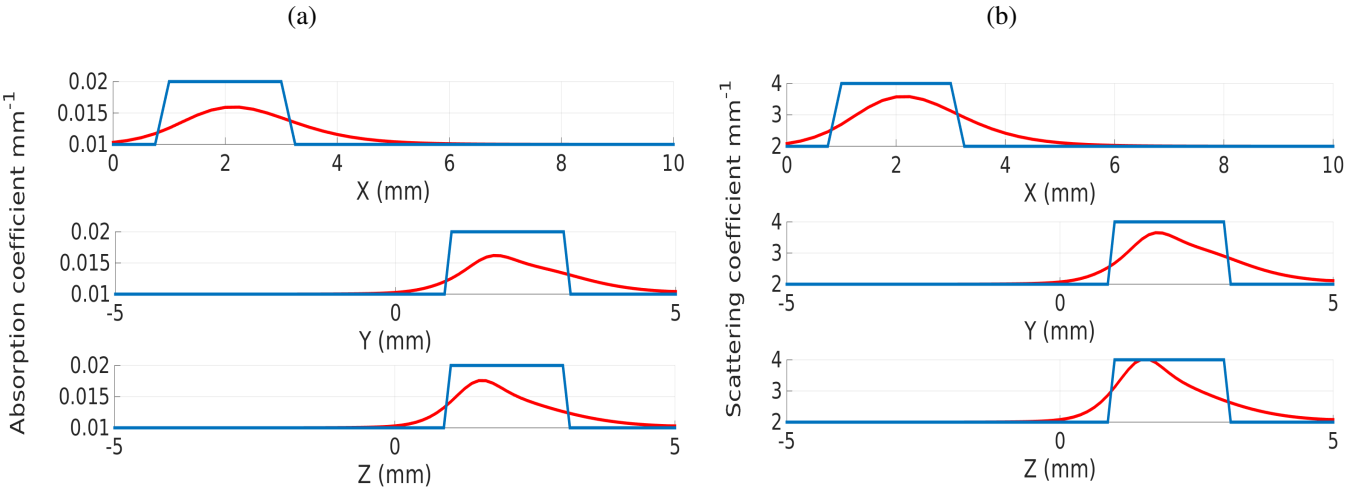

Figure 5: Simultaneous reconstruction of μ_a and μ_s for the fourth test case : the reconstructed profiles (red lines) passing through the center of the inclusion along the x, y and z axis for the absorption (a) and scattering (b) coefficients. The blue lines indicate the exact profiles.

accuracy of the inclusion. It can be seen that the algorithm has well fitted the optical values of the inclusion with the exact solution in both parameters. The center of the reconstructed inclusion (for both μ_a and μ_s) has been accurately located in depth (x_{inc} = 2 mm) while its positions along the y and z axis were slightly underestimated. The relative estimation errors of the inclusion for μ_a and μ_s are respectively ε_{μ_a} = 27.85% and ε_{μ_s} = 20.74%. The superior quality for μ_s can be explained by the more pronounced underestimation in the μ_a image. This is mainly due to the fact that the μ_s coefficient is more sensitive to the predicted boundary data than the μ_a coefficient.[30] Compared to the previous test case, the relative error was smaller (ε_{μ_s} = 15.86%) when assuming g and μ_a to be known because the ill-conditioning of the inverse problem was reduced by decreasing its under-determinate nature which explains the better image quality. However, the present fourth case illustrates more realistic clinical scenarios and avoid having prior knowledge about the biological tissues.

3.2 Small domain reconstruction

In this section, the performance of the algorithm is examined for a small domain size. The original phantom to be reconstructed is now a cube of 4 mm each side. The computational domain was discretized with 68,921

nodes and 384,000 tetrahedral elements for reconstruction. 320 detectors readings were generated on the western surface using a finer mesh of 746,691 nodes. In this case, the phantom contains a small cylindrical heterogeneity in scattering coefficient (Fig. 6) while μ_a and g are constant. The latter (1 mm of diameter along the x axis and 4 mm of length along the y axis) is embedded in the same homogeneous background as previously and centered at (1, 0, 0). The exact μ_s^* value inside the inclusion was set to 4 mm^{-1}. Seven Laser spots at 600 MHz are equally separated by 0.5 mm and positioned in the planes: z = -0.5 mm, z = 0 mm and z = 0.5 mm leading to 21 collimated sources (see Fig. 6).

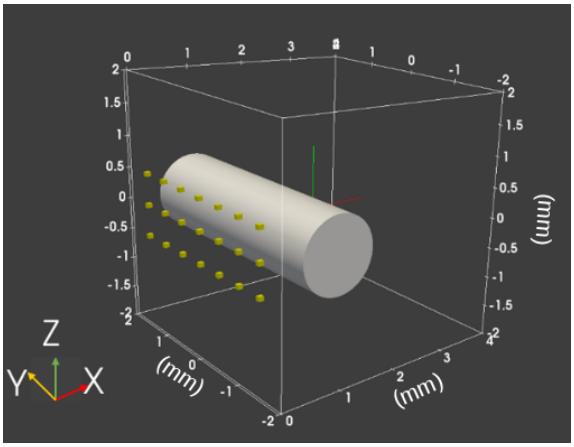

Figure 6: Original phantom. A cylindrical tumoral inclusion centered at (1, 0, 0) is embedded in a background medium : μ_a = 0.01 mm^{-1}, μ_s = 2 mm^{-1} and g = 0.8. The yellow boxes on the western boundary (regularly spaced) represent the 21 Laser shots.

The stopping criterion was satisfied after 16 iterations and the reconstructed image is displayed in Fig. 7. As shown in Fig. 7a, the algorithm has successfully reconstructed the cylindrical shape of the inclusion. Figure 7b shows the reconstructed volumetric image of the μ_s coefficient inside the medium. It can be seen that the retrieved values are spatially well fitted with the original position and the maximum value recorded reaches 3.5 mm^{-1} against 4 mm^{-1}. The relative estimation errors are respectively 31.50 % and 9.9% for the inclusion and the background. This result demonstrates the ability of the algorithm to reconstruct simultaneously the shape and the optical values of the inclusion. This was accomplished without any implementation of a specific shape-based reconstruction method.[31] It should be mentioned that the commonly used Diffusion Equation fail to predict the light propagation in such situation because the reflected data were collected at distances less than 3 l_{tr} away from the source.[9]

(a) (b)

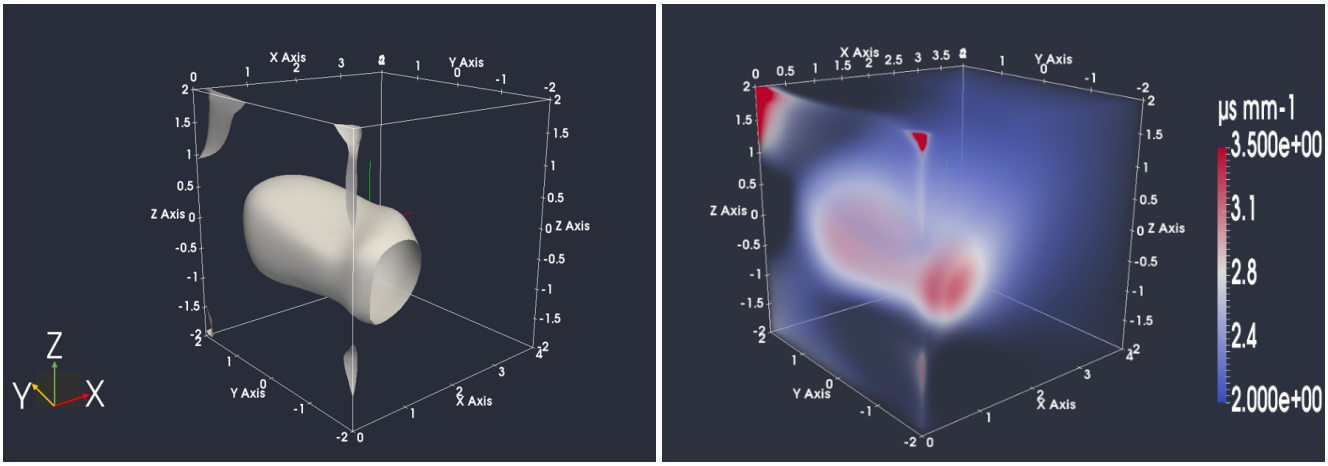

Figure 7: Reconstructed μ_s image for the cylindrical inclusion case. (a) shows the 3D cylindrical boundary thresholded at 3 mm^{-1} (b) depicts the interior volumetric spatial distribution of the scattering retrieved values.

3.3 g-factor reconstruction

As mentioned earlier, we attempted to reconstruct the spatial distribution of the anisotropy factor g of the H-G phase function. In our previous publication based on the sensitivity analysis,[30] we have shown that this factor has a notable effect on the light propagation. A small perturbation of g leads to a more important variation on the backscattering light compared to the one induced by μ_a or μ_s perturbations. This represents an important advantage because the optical contrast levels are believed to be weak between normal and tumoral tissues.[32] Furthermore, as the g values of biological tissues are close to unity, the contrast levels in this factor are expected to be very low. It is known that the light propagation becomes isotropic ($g = 0$) when the photons have traveled several transport mean-free path in the medium ($\approx 8 \times l_{tr}$).[33] Hence, the spatial domain to be reconstructed for the g-factor should not be deeper than approximately $8 \times l_{tr}$ with respect to the probed surface. The dimensions of the previous phantom represent a suitable example of the g-factor reconstruction assessment. Herein, the original cubic medium contains a spherical heterogeneity with 1 mm of a diameter which is embedded at $X = 1$ mm in depth, $Y = 1$ mm and $Z = 1$ mm. The source was positioned at (0, 0.5, 0.5) on the western surface of the phantom.

In order to verify that the spatial variation of g is not be attributed to a variation of μ_s' itself, a preliminary test case is addressed. It considers two combinations of μ_s and g leading to a constant value of μ_s' in the medium. The optical properties of the background were unchanged, as mentioned in subsection 3.1, while $\mu_a = 0.01$ mm^{-1}, μ_s

= 4 mm^{-1} and g = 0.9 were assigned to the inclusion. The reconstructed image of g is depicted in Fig. 8. The last shows the ability of the algorithm to spatially recover the heterogeneity in the g-factor even where the μ_s' coefficient is constant in the medium. It can be seen that the obtained μ_s' coefficient is constant between the background and the inclusion. This implies that the spatial variation of g cannot be caused by a variation of μ_s' itself. The g-factor can thus be independently reconstructed and separated from μ_s with the RTE inverse solver.

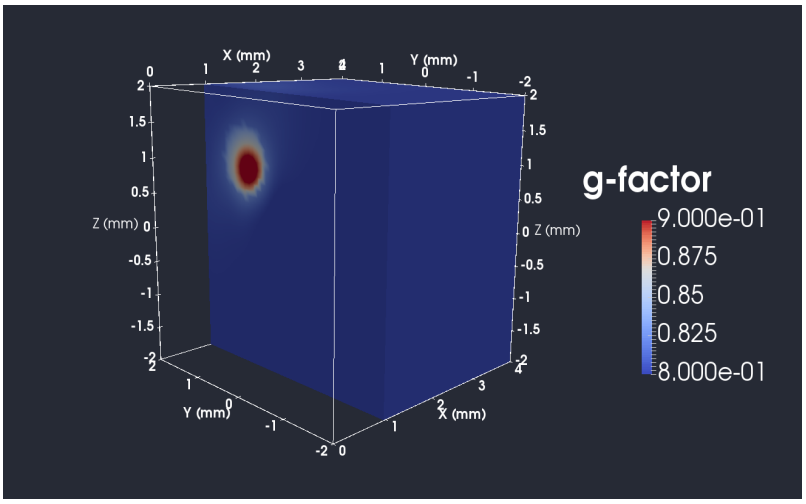

Figure 8: Preliminary test case, reconstruction of the anisotropy factor g when the reduced scattering coefficient $\mu_s^{'}$ is uniform in the phantom.

The robustness of the algorithm is then examined in presence of some issues encountered in optical tomography such as contrast level, heterogeneous background, inclusion depth, initial guess, noise level, layered medium and crosstalk between g and μ_s. These issues are assessed through several test cases. For all the test cases, expect the crosstalk case, only the g-factor is spatially reconstructed while the μ_a and μ_s coefficients are fixed at their homogeneous background values.

The first one considers a relatively high contrast inclusion with + 18% (g^* = 0.95) with respect to the homogeneous background value (g = 0.8). The minimization has been satisfied after 10 iterations. The obtained 3D slices at the x = 1 mm, y = 1 mm and z = 1 mm planes are plotted in the Figs. 9a-c, respectively. The reconstructed profiles passing through the center of the inclusion are depicted in Fig. 9d. It is readily seen that the inclusion has been located at approximately the right position (x_{inc} = 0.9 mm, y_{inc} = 0.9 mm, z_{inc} = 0.9 mm) and the circular shape was clearly reconstructed. However, the maximum retrieved value inside the inclusion is somehow underestimated compared to its original value with an error ε = 14.4% (Fig. 9d). As expected, the computation cost is

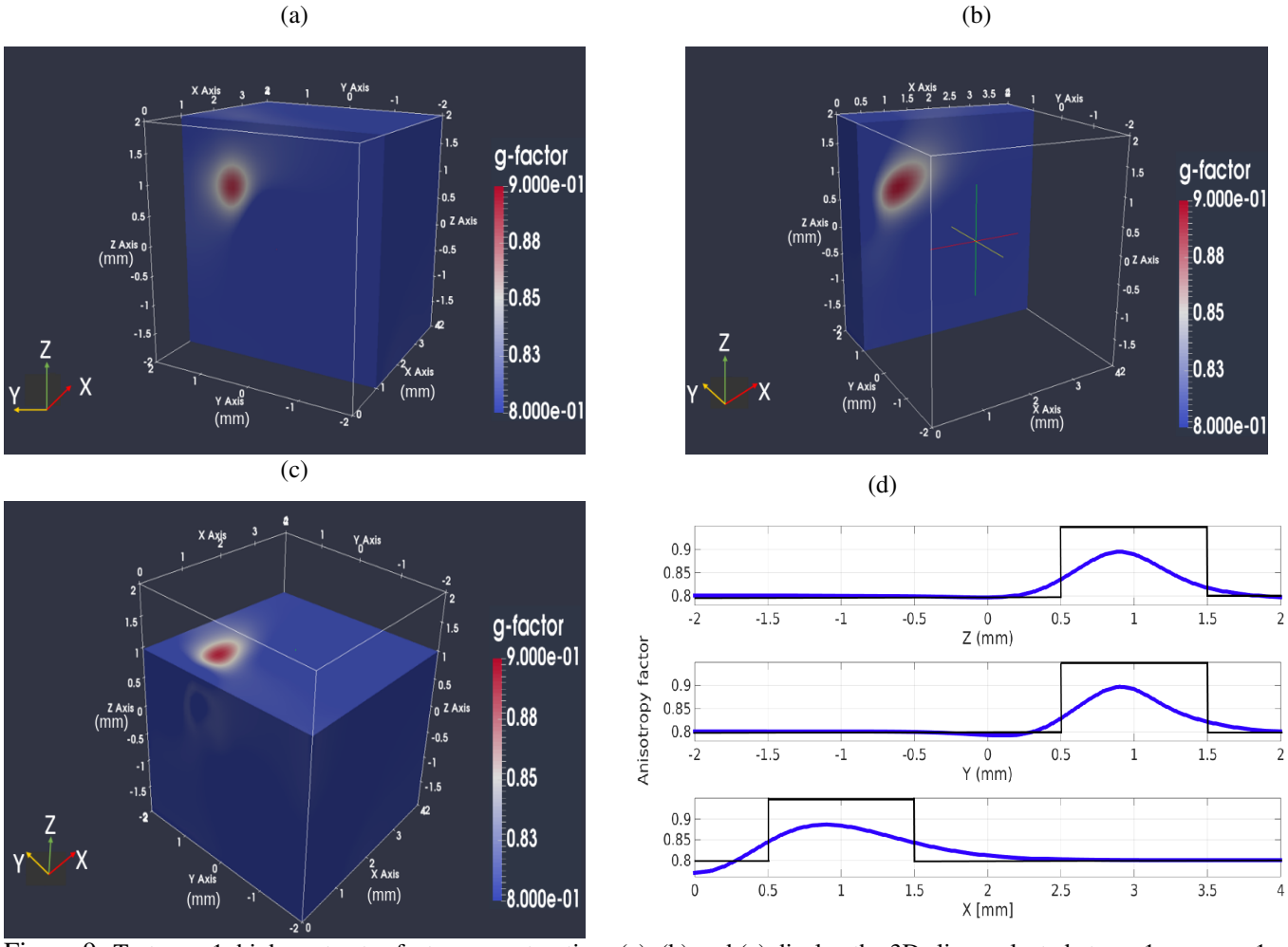

Figure 9: Test case 1, high contrast g-factor reconstruction. (a), (b) and (c) display the 3D slices selected at x = 1 mm, y = 1 mm and z = 1 mm, respectively. (d) represents the recovered profiles passing by the inclusion center along the x - y - and z - axis.

expensive as each iteration in the inversion procedure has required 100 min to calculate the gradient. In order to assess the convergence quality of the algorithm, the reconstructed profiles obtained at the 2^{th}, 4^{th} and 6^{th} iterations are displayed in the Fig. 10. The results show that the algorithm can accurately locate the inclusion from only the second iteration. The suspect area can then be defined very quickly (in a few minutes) and might be exploited as a prior structural knowledge.

The second test considers a heterogeneous background containing two laterally separated inclusions with low contrast levels of $\pm$ 6%. The first one (g^* = 0.75) was placed at (1, 1, 1) while the second one (g^* = 0.85) was positioned at (1, -0.5, 1). The stop criterion was satisfied at the $38th$ iteration and the reconstructed 3D medium is shown in Fig. 11. Despite the low contrast levels, the algorithm was still able to spatially locate and reveal the two closed heterogeneities in the medium. Compared to the previous test case, the quantitative accuracy was improved

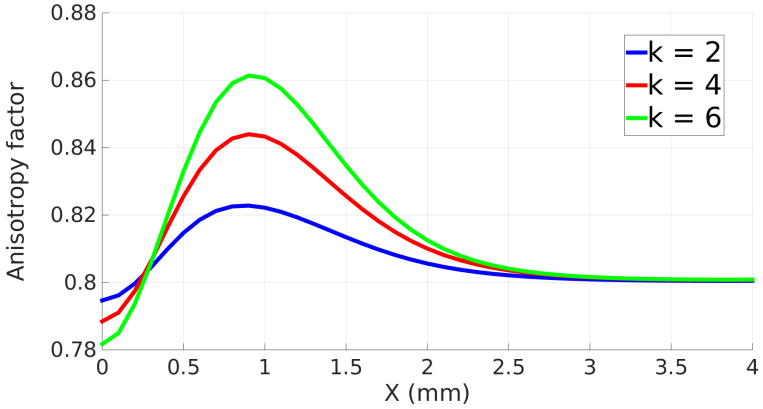

Figure 10: The reconstructed profiles along x axis passing by the inclusion center (y = 1 mm, z = 1 mm) for the three iterations 2^{th}, 4^{th} and 6^{th} of the inverse minimization.

only for the first inclusion (blue) where the relative estimation error decreased to ε = 3.39 %. This is because the discrepancy between the initial value and the exact solution of the inverse problem is reduced when the contrast level is low, therefore making the estimation more accurate. On the other hand, the retrieved values in the other inclusion (red) were under-estimated the maximal value reaching $\approx$ 0.82 against 0.85 (Fig. 11). This is mainly due to its localization within a low sensitivity region with respect to the collimated source.

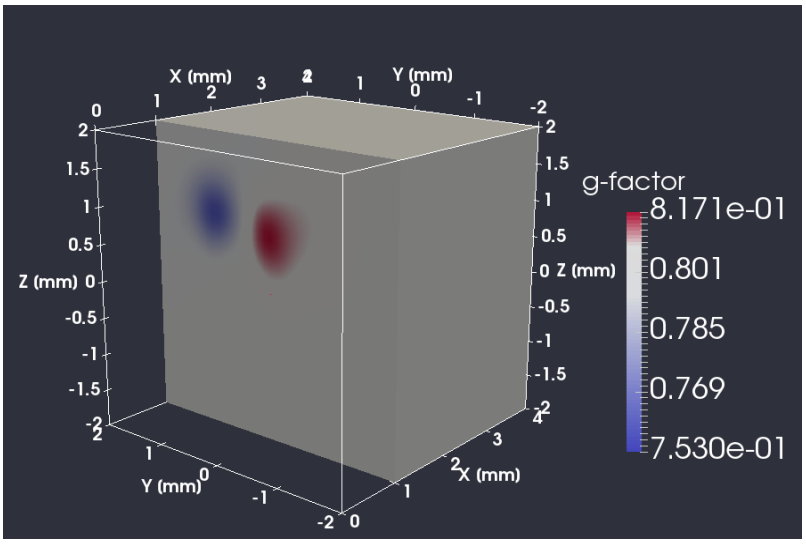

Figure 11: Test case 2, reconstruction of a heterogeneous background containing two inclusions laterally separated. The blue inclusion (1, 1, 1) presents a low contrast of - 6% while the red one (1, -0.5, 1) presents a contrast of + 6% with respect to the homogeneous value.

It is well known that the light intensity drops off severely with depth making the detection of deep inclusions more difficult in optical imaging. In the third test case, we evaluated the capacity of the algorithm to localize deep heterogeneities in the g-factor and the effect of depth on the relative error. The low contrast inclusion with $g^* = 0.75$ is reconstructed at different depth, namely 1.5 mm, 2 mm and 3 mm. The corresponding results are shown in Figs. (12a - c), respectively. Fig. 12d shows the variation of the relative estimation error with respect to the inclusion depth. It can be seen that the reconstruction quality is worse as the inclusion is located deeper since its influence on the boundary reflected data becomes very weak (see Fig. 12d). The images show that the algorithm is still able to qualitatively recover the circular shape of the inclusion located at 3 mm depth as well as its location in the medium. However, its quantitative accuracy decreases with a relative error of 6.6 $\%$. Moreover, the spatial contrast in the medium is lower compared to the other depths (Figs. 12a-12c).

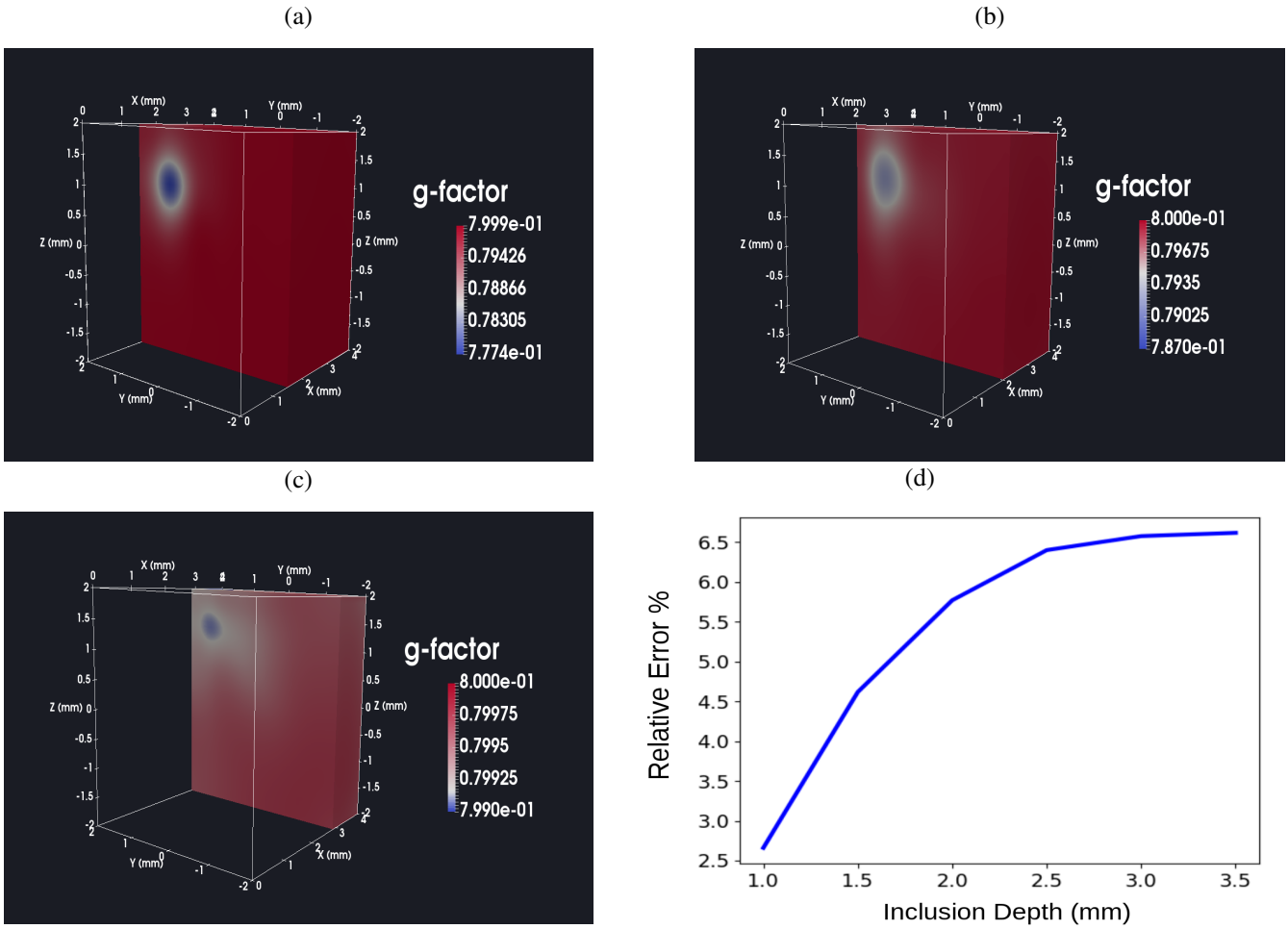

Figure 12: Test case 3, reconstruction of a low contrast (-6$\%$) inclusion at different depth : (a), (b) and (c) display the 3D slices at depths 1.5 mm, 2 mm and 3 mm, respectively. (d) represents the variation of the relative error versus inclusion depth.

One of the gradient-based optimization schemes drawbacks is the choice of the initial estimate which should not be far away from the exact solution of the iterative procedure. Usually, this estimate is described by the homogeneous optical properties of the original background. The robustness of the algorithm on different initial guesses g^0 is examined with the fourth test case. It consists to reconstruct an inclusion with $g^* = 0.75$ embedded in a homogeneous background of $g = 0.8$ under three examples of initial guesses $g^0 = 0.8$, $g^0 = 0.82$ and $g^0 = 0.85$. The retrieved profiles along x, y and z axis are shown in figure 13. The relative estimation errors of inclusion and background are listed in Table 1.

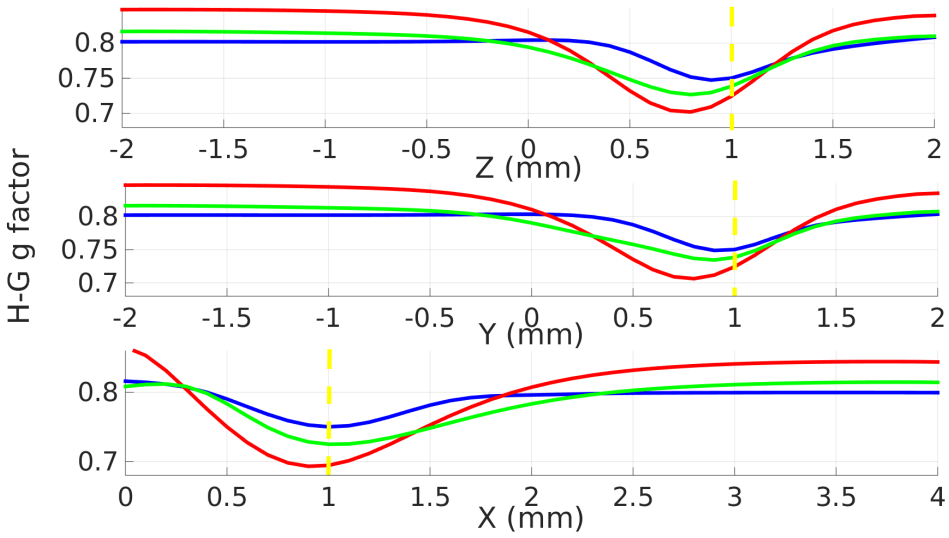

Figure 13: Test case 4, the reconstructed profiles passing through the center position of the inclusion along the x, y and z axis for the three different initial estimates. The red, green and blue profiles correspond to $g^0 = 0.85$, $g^0 = 0.82$ and $g^0 = 0.80$, respectively. The dashed yellow lines indicate the center position of the inclusion.

	Inclusion			Background	
Initial Guess	ε_g (%)	$\varepsilon_{position}$ (%)	$\hat{g}_{minimum}$	ε_g (%)	$\hat{g}_{average}$
$g^0 = 0.8$	2.66%	8.1 %	0.75	0.88%	0.7981
$g^0 = 0.82$	3.63%	14.4 %	0.73	1.82%	0.8131
$g^0 = 0.85$	4.46%	21.21 %	0.68	5.41%	0.8420

Table 1: Test case 4, the relative errors of background and inclusion for the three different initial guesses. $\hat{g}_{minimum}$ represents the minimum estimated value of g-factor and $\hat{g}_{average}$ denotes its estimated mean value.

Qualitatively, the algorithm has correctly found the spatial localization of the inclusion when the initial value was different from the original background value (see Fig. 13). The relative estimation errors of the g-factor increase from 2.66 % to 4.46 % for the inclusion and from 0.88 % to 5.41 % for the background when the homogeneous initial value g^0 was chosen from 0.8 to 0.85, respectively (see Tab. 1). Furthermore, the relative position errors of

the inclusion increase and its retrieved values becomes more under-estimated (from $\hat{g}_{minimim}$ = 0.75 to $\hat{g}_{minimim}$ = 0.68) when g^0 moves away from the original background value. Additionally, the retrieved mean values of the reconstructed background don't change sufficiently and remain near to the initial homogeneous value (see Tab. 1). The noisy data are unavoidable in real clinical scenarios. It is important to check the effect that noise has on the reconstruction quality of the g-factor. In the fifth test study, the simulated measurement data are corrupted with four different noise levels: 1%, 3%, 6%, and 10%. The noise was added to the complex simulated reflectance (module and phase shift). The medium contains one inclusion positioned at 1 mm depth with g^* = 0.75. The relative errors of inclusion and background with the iterations numbers of the algorithm are given in Table 2. The latter shows that the estimation accuracy of both inclusion and background decreases when the noise level increases. As expected, higher noise levels on the boundary data lead to quality image degradation. The background error becomes significantly high at 10% (ε = 8.05$\%$) compared to the error obtained at 1% (ε = 0.88 $\%$). This is because detection occurred on the surface. Therefore, edges artifacts and perturbations become more pronounced in the whole reconstructed medium at larger noise level. On the other hand, the optimization procedure reached the stop criterion faster as the noise level is higher since the algorithm converged around random values. This computational feature was often encountered for gradient-based algorithms.[18]

	Noise levels			
	1 %	3 %	6 %	10 %
ε of inclusion (%)	2.66	3.53	7.12	13.51
ε of background (%)	0.88	1.75	4.43	8.05
Number of iterations	29	20	13	7

Table 2: Test case 5, the relative estimation errors ε of background and inclusion with the iterations numbers of the reconstruction algorithm for the 4 different noise levels on the reflected data.

The characterization of multi-layered media representing several anatomical structures of biological tissues has frequently been studied in the literature.[34,35] However, it was mainly restricted to reflectance spectroscopic applications[36,37] where the layer thickness is often assumed to be known. In the sixth test case, the reconstruction of the g-factor is studied for a two-layered phantom which mimics the epidermis and dermis of human skin tissue. The layers thickness are considered to be unknown and not used as a prior information in the reconstruction algorithm. The optical properties and thicknesses of the two layers are given in Table 3. The phantom is illuminated as in the

cylindrical example (section 3.2).

Optical properties	Epidermis	Dermis
Absorption μ_a (mm^{-1})	0.19	0.13
Scattering μ_s (mm^{-1})	18.95	11.65
Thickness (mm)	1	3

Table 3: Thickness and optical properties of epidermis and dermis at 785 nm extracted from [38].

The g value of the epidermis ($g^{epidermis}$ = 0.75) is assumed to be different from the dermis (g^{dermis} = 0.8) in order to consider endogenous spatial variation within the skin tissue.

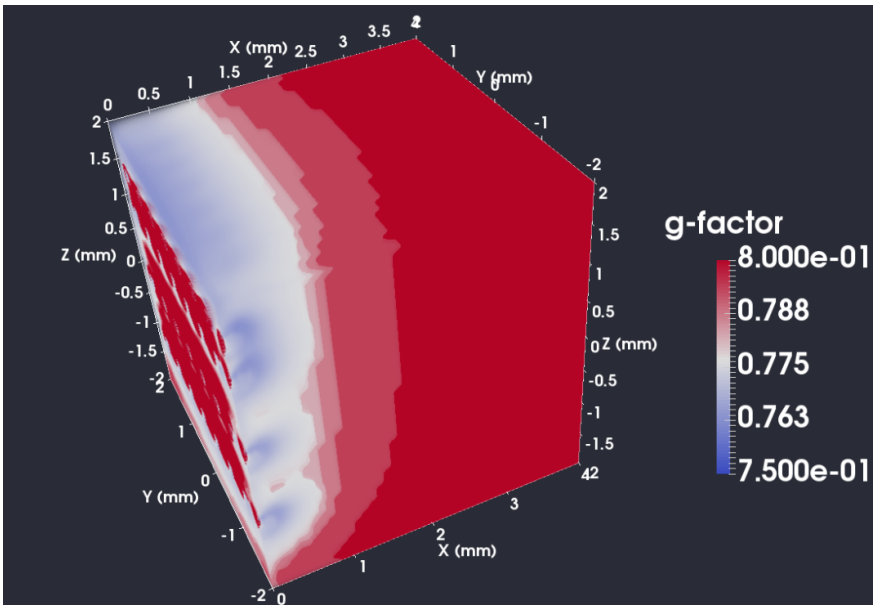

Figure 14: Test case 6, reconstruction of a two-layered phantom representing the human skin tissue composed of dermis (1 mm) and epidermis (3 mm).

Figure 14 shows the spatial distribution of the recovered volumetric g-factor. As expected, the reconstructed phantom has two layers. The relative errors of the retrieved values are 6.4 % and 0.9 % for the epidermis and dermis respectively. The error of the first layer is higher due to the artifacts at the illuminated boundary. Additionally to the reasonable quantitative accuracy, the algorithm, not aware of the internal structure, has also correctly provided the layer thickness of the epidermis. The obtained result can be considered as an illustration for pre-clinical imaging of small-layered media.

To date, the simultaneous reconstruction of μ_s and g-factor has not been considered in the literature for optical imaging. In order to study and mime the crosstalk between the scattering parameters, the final test case considers two different examples. In this case, all boundaries nodes are taken as detection locations for the inversion. For

the first example, the inclusion varies only in the anisotropy factor (g^* = 0.85) while it represents a heterogeneity only in scattering coefficient (μ_s^* = 4 mm^{-1}) for the second example. The reconstructed results are depicted in Fig. 15. As shown, the reconstructed profile was spatially well fitted with the original distribution for the first example. The maximum local value retrieved in the g inclusion has reached 0.84 against 0.85. For the second example, the algorithm has localized the μ_s inclusion in its exact position but the quantitative accuracy was very underestimated. Indeed, the maximum value has reached only 2.5 mm^{-1} against 4 mm^{-1}. The superiority in the quality reconstruction of the g-factor can be explained by the high sensitivity of this factor on the boundary data. It can be seen that the crosstalk effect induced in each parameter was insignificant.

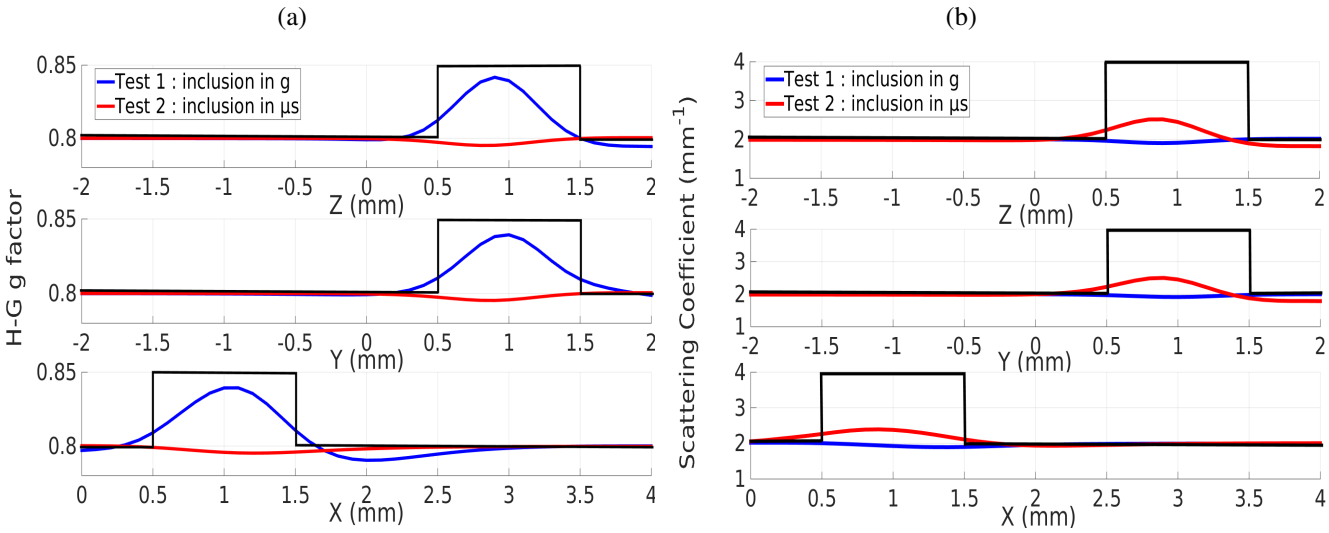

Figure 15: The final test case, simultaneous reconstruction of μ_s and g. The reconstructed profiles passing through the center position of the inclusion along the x, y and z axis for the anisotropy factor (a) and for the scattering coefficient (b). The black solid profils represent the original position of the inclusion.

It should be noted that the reconstruction of g would not have been possible with the Diffusion Equation since the anisotropy information is lost by considering the μ_s' coefficient[39] where the g value is given. Despite the several studies of 3D optical imaging that were conducted with the RTE, none has presented the reconstruction of the g-factor, for the authors best knowledge. Although the study was carried out with synthetic data, it nevertheless constitutes an important first step (numerical validation) in the imaging of g-factor for optical imaging. The data were generated with the RTE-based forward model, it is important, in the next step, to synthesize the back-scattered intensities with an another modality such as Monte-Carlo simulations to perform reconstructions. This would allow using arbitrary phase-functions in order to assess the impact of the phase-function mismatches of the g quality

reconstruction. The clinical potential of the method particularly concerns small tissue imaging to detect superficial lesions such as cutaneous tumors (melanoma), finger joints or small animal imaging and even for biopsies characterization. The g-factor can then be considered as a potential endogenous contrast biomarker which provides additional intrinsic information beside μ_a and μ_s.

4 Conclusion

A 3D optical reconstruction algorithm based on the RTE-based forward model was presented to detect tumor-like inclusions. The algorithm can reconstruct and localize small inclusions with a reasonable quality when only one tissue surface is probed and within situations in which the commonly used Diffusion Equation is not valid. Furthermore, we highlighted the performance of the algorithm to retrieve simultaneously the inclusions shapes (spherical and cylindrical) and the spatial optical values. The main novelty of this work is the reconstruction of the spatial distribution of the anisotropy factor of the Henyey-Greenstein phase function. This was made possible thanks to the combination of the RTE-based forward model, the adjoint model, and the parallel computing. The algorithm was proven to be robust in recovering a heterogeneity in g-factor in presence of some issues such as low or high contrast level, inclusion depth, heterogeneous background and with different initial guesses and noise levels. The simultaneous reconstruction of μ_s and g was also achieved with a reasonable quality while the crosstalk between the two parameters was weak. Moreover, the algorithm was able to retrieve a spatial map of the thickness and g values of a two-layered phantom that mimics the optical properties of epidermis and dermis. This work was a necessary preliminary study before using the present algorithm with experimental boundary data and performing real small-tissues imaging. Although the Open MP and MPI libraries have allowed us to considerably reduce the reconstruction times, they would still need to be accelerated for clinical diagnostic applications. To this end, parallelization based on GPU (Graphics Processing Unit) is envisaged for some calculations of the RTE inverse solver. The simultaneous reconstruction of the three optical properties μ_a, μ_s and g-factor is currently under investigation. That can be an important issue for optical tomography which it is not easy due to the ill-posed inverse problem and to the difference in nature, units, and sensitivities of the parameters on the boundary data.

Disclosure of Conflicts of Interest

The authors have no relevant financial interests in this article and no potential conflicts of interest to disclose.

Bibliography

[1] Dehghani Hamid, Matthew E. Eames, phaneendra k. yalavarthy, Davis Scott C., Srinivasan Subhadra, Carpenter Colin M., Pogue Brian W., and Paulsen Keith D. Near infrared optical tomography using nirfast: Algorithm for numerical model and image reconstruction. *Communications in Numerical Methods in Engineering*, 25(6):711–732, 2008.

[2] Andreas H Hielscher, Raymond E Alcouffe, and Randall L Barbour. Comparison of finite-difference transport and diffusion calculations for photon migration in homogeneous and heterogeneous tissues. *Physics in Medicine & Biology*, 43(5):1285, 1998.

[3] A. H. Hielscher, H. K. Kim, L. D. Montejo, S. Blaschke, U. J. Netz, P. A. Zwaka, G. Illing, G. A. Muller, and J. Beuthan. Frequency-domain optical tomographic imaging of arthritic finger joints. *IEEE Transactions on Medical Imaging*, 30(10):1725–1736, Oct 2011.

[4] Zhen Yuan, Xin-Hua Hu, and Huabei Jiang. A higher order diffusion model for three-dimensional photon migration and image reconstruction in optical tomography. *Physics in Medicine & Biology*, 54(1):65, 2009.

[5] Xuejun Gu, Kui Ren, and Andreas H. Hielscher. Frequency-domain sensitivity analysis for small imaging domains using the equation of radiative transfer. *Appl. Opt.*, 46(10):1624–1632, Apr 2007.

[6] Steven L Jacques. Optical properties of biological tissues: a review. *Physics in Medicine & Biology*, 58(11):R37, 2013.

[7] Richard Van Hillegersberg, John W. Pickering, Aalders Maurice, and Beek Johan F. Optical properties of rat liver and tumor at 633 nm and 1064 nm: Photofrin enhances scattering. *Lasers in Surgery and Medicine*, 13(1):31–39, 1993.

[8] Christoph-Thomas Germer, Roggan Andre, Joerg P. Ritz, Isbert Christoph, Albrecht Dirk, Muller Gerhard, and Buhr Heinz J. Optical properties of native and coagulated human liver tissue and liver metastases in the near infrared range. *Lasers in Surgery and Medicine*, 23(4):194–203, 1998.

[9] T Durduran, R Choe, W B Baker, and A G Yodh. Diffuse optics for tissue monitoring and tomography. *Reports on Progress in Physics*, 73(7):076701, 2010.

[10] Alexander D. Klose and Andreas H. Hielscher. Iterative reconstruction scheme for optical tomography based on the equation of radiative transfer. *Medical Physics*, 26(8):1698–1707, 1999.

[11] T. Tarvainen, M. Vauhkonen, and S.R. Arridge. Gauss-newton reconstruction method for optical tomography using the finite element solution of the radiative transfer equation. *Journal of Quantitative Spectroscopy and Radiative Transfer*, 109(17):2767 – 2778, 2008.

[12] Yaobin Qiao, Hong Qi, Qin Chen, Liming Ruan, and Heping Tan. Multi-start iterative reconstruction of the radiative parameter distributions in participating media based on the transient radiative transfer equation. *Optics Communications*, 351:75 – 84, 2015.

[13] Gassan S. Abdoulaev and Andreas H. Hielscher. Three-dimensional optical tomography with the equation of radiative transfer. *Journal of Electronic Imaging*, 12:12 – 12 – 8, 2003.

[14] Alexander D. Klose and Andreas H. Hielscher. Optical tomography using the time-independent equation of radiative transferâĂŤpart 2: inverse model. *Journal of Quantitative Spectroscopy and Radiative Transfer*, 72(5):715 – 732, 2002.

[15] Kui Ren, Guillaume Bal, and Andreas H. Hielscher. Frequency domain optical tomography based on the equation of radiative transfer. *SIAM Journal on Scientific Computing*, 28(4):1463–1489, 2006.

[16] Hyun Keol Kim and André Charette. A sensitivity function-based conjugate gradient method for optical tomography with the frequency-domain equation of radiative transfer. *Journal of Quantitative Spectroscopy and Radiative Transfer*, 104(1):24 – 39, 2007.

[17] Yaobin Qiao, Hong Qi, Qin Chen, Liming Ruan, and Heping Tan. An efficient and robust reconstruction method for optical tomography with the time-domain radiative transfer equation. *Optics and Lasers in Engineering*, 78:155 – 164, 2016.

[18] Alexander D Klose and Andreas H Hielscher. Quasi-newton methods in optical tomographic image reconstruction. *Inverse Problems*, 19(2):387, 2003.

[19] Jenni Heino, Simon Arridge, Jan Sikora, and Erkki Somersalo. Anisotropic effects in highly scattering media. *Phys. Rev. E*, 68:031908, Sep 2003.

[20] F. Asllanaj, S. Contassot-Vivier, A. Hohmann, and A. Kienle. Light propagation in biological tissue. *Journal of Quantitative Spectroscopy and Radiative Transfer*, 224:78 – 90, 2019.

[21] Ahmad Addoum, Olivier Farges, and Fatmir Asllanaj. Optical properties reconstruction using the adjoint method based on the radiative transfer equation. *Journal of Quantitative Spectroscopy and Radiative Transfer*, 204:179 – 189, 2018.

[22] Michel Kern. Problèmes inverses : aspects numériques. Lecture, September 2002.

[23] O. Balima, J. Boulanger, A. Charette, and D. Marceau. New developments in frequency domain optical tomography. part ii: Application with a l-bfgs associated to an inexact line search. *Journal of Quantitative Spectroscopy and Radiative Transfer*, 112(7):1235 – 1240, 2011.

[24] Fatmir Asllanaj, Sylvain Contassot-Vivier, André Liemert, and Alwin Kienle. Radiative transfer equation for predicting light propagation in biological media: comparison of a modified finite volume method, the monte carlo technique, and an exact analytical solution. *Journal of Biomedical Optics*, 19:19 – 19 – 11, 2014.

[25] J. P. Culver, R. Choe, M. J. Holboke, L. Zubkov, T.Durduran, A. Slemp, V. Ntziachristos, B. Chance, and A. G.Yodh. Three dimensional diffuse optical tomography in the parallel plane transmission geometry: Evaluation of a hybrid frequency domain/continuous wave clinical system for breast imaging. *Medical Physics*, 30(2):235–247, 2003.

[26] Gultekin Gulsen, Bin Xiong, Ozlem Birgul, and Orhan Nalcioglu. Design and implementation of a multifrequency near-infrared diffuse optical tomography system. *Journal of Biomedical Optics*, 11:11 – 11 – 10, 2006.

[27] Uwe J. Netz, Jurgen Beuthan, and Andreas H. Hielscher. Multipixel system for gigahertz frequency-domain optical imaging of finger joints. *Review of Scientific Instruments*, 79(3):034301, 2008.

[28] Chengyu Li, Raweewan Liengsawangwong, Haesun Choi, and Rex Cheung. Using a priori structural information from magnetic resonance imaging to investigate the feasibility of prostate diffuse optical tomography and spectroscopy: A simulation study. *Medical Physics*, 34(1):266–274.

[29] Zhen Yuan, Qizhi Zhang, Eric S. Sobel, and Huabei Jiang. High-resolution x-ray guided three-dimensional diffuse optical tomography of joint tissues in hand osteoarthritis: Morphological and functional assessments. *Medical Physics*, 37(8):4343–4354.

[30] M. Marin, F. Asllanaj, and D. Maillet. Sensitivity analysis to optical properties of biological tissues subjected to a short-pulsed laser using the time-dependent radiative transfer equation. *Journal of Quantitative Spectroscopy and Radiative Transfer*, 133:117 – 127, 2014.

[31] Athanasios Zacharopoulos, Martin Schweiger, Ville Kolehmainen, and Simon Arridge. 3d shape based reconstruction of experimental data in diffuse optical tomography. *Opt. Express*, 17(21):18940–18956, Oct 2009.

[32] Huabei Jiang, Keith D. Paulsen, Ulf L. Osterberg, Brian W. Pogue, and Michael S. Patterson. Simultaneous reconstruction of optical absorption and scattering maps in turbid media from near-infrared frequency-domain data. *Opt. Lett.*, 20(20):2128–2130, Oct 1995.

[33] Rachid Elaloufi, Rémi Carminati, and Jean-Jacques Greffet. Diffusive-to-ballistic transition in dynamic light transmission through thin scattering slabs: a radiative transfer approach. *J. Opt. Soc. Am. A*, 21(8):1430–1437, Aug 2004.

[34] Robert J Hunter, Michael S Patterson, Thomas J Farrell, and Joseph E Hayward. Haemoglobin oxygenation of a two-layer tissue-simulating phantom from time-resolved reflectance: effect of top layer thickness. *Physics in Medicine & Biology*, 47(2):193, 2002.

[35] Alwin Kienle and Thomas Glanzmann. In vivo determination of the optical properties of muscle with time-resolved reflectance using a layered model. *Physics in Medicine & Biology*, 44(11):2689, 1999.

[36] Te-Yu Tseng, Chun-Yu Chen, Yi-Shan Li, and Kung-Bin Sung. Quantification of the optical properties of two-layered turbid media by simultaneously analyzing the spectral and spatial information of steady-state diffuse reflectance spectroscopy. *Biomed. Opt. Express*, 2(4):901–914, Apr 2011.

[37] Quan Liu and Nirmala Ramanujam. Scaling method for fast monte carlo simulation of diffuse reflectance spectra from multilayered turbid media. *J. Opt. Soc. Am. A*, 24(4):1011–1025, Apr 2007.

[38] Arka Bhowmik, Ramjee Repaka, Subhash C. Mishra, and Kunal Mitra. Analysis of radiative signals from normal and malignant human skins subjected to a short-pulse laser. *International Journal of Heat and Mass Transfer*, 68:278 – 294, 2014.

[39] Michael Chu and Hamid Dehghani. Image reconstruction in diffuse optical tomography based on simplified spherical harmonics approximation. *Opt. Express*, 17(26):24208–24223, Dec 2009.